Geophysical Research Letters

RESEARCH LETTER
10.1029/2019GL085999

Six-Axis Ground Motion Measurements of Caldera Collapse at Kīlauea Volcano, Hawai'i—More Data, More Puzzles?

J. Wassermann[1], F. Bernauer[1], B. Shiro[2], I. Johanson[2], F. Guattari[3], and H. Igel[1]

[1]Department of Earth and Environmental Sciences, LMU Munich, Munich, Germany, [2]USGS Hawaiian Volcano Observatory, Hilo, HI, USA, [3]iXblue, St-Germain-en-Laye, France

Key Points:
- First recording of dynamic rotational and translational motion over a very broad frequency range in close distance to a volcano-related earthquake
- Complete reconstruction of ground motion history using six component recordings
- Rotational motion recordings reveal a large influence of local site conditions and/or detailed source effects which are not perceptible in traditional translational recordings

Correspondence to:
J. Wassermann,
j.wassermann@lmu.de

Citation:
Wassermann, J., Bernauer, F., Shiro, B., Johanson, I., Guattari, F., & Igel, H. (2020). Six-axis ground motion measurements of caldera collapse at Kilauea Volcano, Hawai'i—More Data, More Puzzles? *Geophysical Research Letters*, *47*, e2019GL085999. https://doi.org/10.1029/2019GL085999

Received 28 OCT 2019
Accepted 18 FEB 2020
Accepted article online 20 FEB 2020

©2020. The Authors.
This is an open access article under the terms of the Creative Commons Attribution License, which permits use, distribution and reproduction in any medium, provided the original work is properly cited.

Abstract Near-field recordings of large earthquakes and volcano-induced events using traditional seismological instrumentation often suffer from unaccounted effects of local tilt and saturation of signals. Recent hardware advances have led to the development of the blueSeis-3A, a very broadband, highly sensitive rotational motion sensor. We installed this sensor in close proximity to permanently deployed classical instrumentation (i.e., translational seismometer, accelerometer, and tiltmeter) at the Hawaiian Volcano Observatory (USGS). There, we were able to record three ~Mw 5 earthquakes associated with large collapse events during the later phase of the 2018 Kīlauea summit eruption. Located less than 2 km from the origins of these sources, the combined six-axis translational and rotational measurements revealed clear static rotations around all three coordinate axes. With these six component recordings, we have been able to reconstruct the complete time history of ground motion of a fixed point during an earthquake for the first time.

Plain Language Summary By combining a traditional seismometer with a fiber optic gyroscope adapted from navigation technology we record for the first time the complete dynamic history of a point motion during strong shaking close to the source of seismic signals. The collapsing crater of Kīlauea leads to static displacements and rotations that help characterizing the geometry of the associated source processes.

1. Introduction

The May to August 2018 eruption of Kīlauea volcano was exceptional in many respects, representing one of the largest eruptions of the volcano in over 200 years (Neal et al., 2019). The complex sequence included a prominent effusive flank eruption, a Mw 6.9 earthquake on 4 May 2018, and episodic caldera collapse at Kīlauea's summit. Sixty-two collapse events occurred from mid-May through early August. Each collapse event, which occurred roughly every 0.5–2 days, was preceded by a swarm of hundreds of volcano-tectonic earthquakes cumulating in a ~Mw 5 earthquake at the time of the caldera collapse. This regular pattern of collapse and swarm seismicity provided an opportunity to test an experimental rotational motion broadband sensor in this unique setting.

A blueSeis-3A rotational motion broadband sensor from iXblue (www.blueseis.com), which is sensitive only to rotational motion, was installed in the Uwekahuna (UWE) station vault of the Hawaiian Volcano Observatory (USGS-HVO) monitoring network (Figure 1c). This vault, located near the HVO, approximately 1.5 km from the epicenters of the ~Mw 5 collapse events, was equipped with a Streckeisen STS-2 broadband seismometer, Kinemetrics EpiSensor accelerometer both accessible via IRIS DMC (USGS, 1956) as well as a nearby installed Jewell Lily borehole tiltmeter and a GNSS sensor. The existing infrastructure at the site accommodated a relatively fast installation of the blueSeis-3A rotational seismometer. The co-location of this instrument in the vault allowed for simultaneous recording and direct comparison of the blueSeis-3A rotational measurements with translational and tilt data from the other instruments in the vault.

A series of recent papers (Bernauer et al., 2014; Donner et al., 2016; Igel et al., 2007; Wassermann et al., 2016) demonstrated how three component rotational combined with three component translational (i.e., six-axis) measurements may help to improve our capability to invert for local (S-wave) velocity, to localize events, and to estimate source mechanisms even in the case of sparse seismic station networks and local tilt effects. The installation of this rotational device so close to large seismic sources created a unique opportunity to test some of these capabilities in a real-world application.

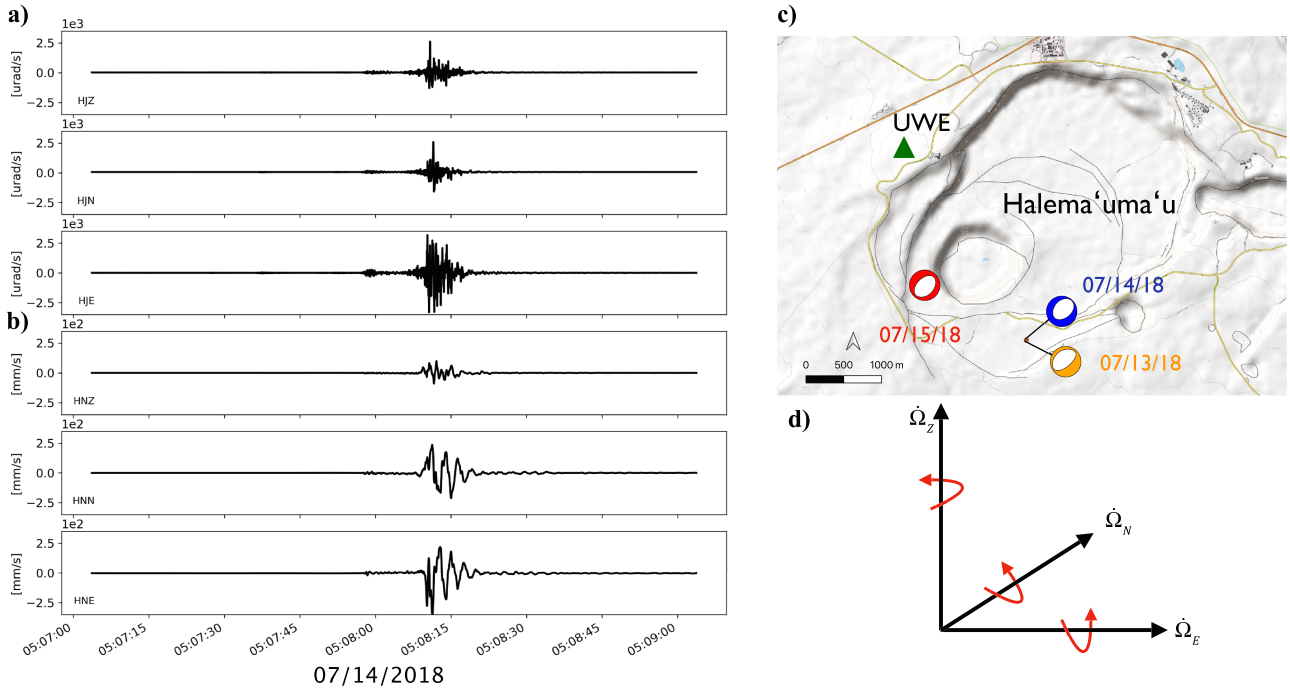

Figure 1. (a) Two minutes of raw rotational blueSeis-3A seismograms of the Mw 5.3 event at 14 July 2018 05:08:03 UTC, (b) corresponding integrated unfiltered, tilt-corrected ground velocity seismograms recorded with the EpiSensor. All data are resampled to a sampling rate of 100 Hz. In (c) the map shows the centroid event epicenters of all three recorded ~Mw 5 events and location of the UWE vault with respect to Halema'uma'u crater (note the 13 July 2018 00:43 event and the event at 14 July 2018 05:08:03 share the same origin) and (d) coordinate system with sense of rotation used in this paper.

2. Data

After the installation of the blueSeis-3A sensor in the UWE vault, we were able to record three individual sequences of collapse events with a combination of three axes of translation and three axes of rotation during July and August 2018. During each of the episodes, the magnitude of earthquakes in the sequences varied from lower than Ml 1 to greater than Mw 5. The resulting wide range of ground motions made it impossible to analyze all seismic events with the broadband STS-2 seismometer. It has a clipping level of 13 mm/s, which makes the records practically unusable during nearby events larger than Mw 3.5, depending on their exact location and depth. In the case of clipped STS-2 recordings, we used data from the EpiSensor strong motion accelerometer instead. Unfortunately, the EpiSensor was not located on the same pier as the STS-2 and the blueSeis-3A but was fixed directly on the floor of the vault next to the pier. This placement may have caused differences in the individual strong motion shaking history of the instruments.

Figures 1a and 1b show an example of the recordings of the Mw 5.3 collapse event on 14 July 2018 at 05:08:03 (UTC). The ground velocity seismograms in Figure 1b are estimated by integrating the tilt-corrected EpiSensor accelerometer data, as the STS-2 records were clipped. The tilt correction was done in the frequency domain using the technique described by Lindner et al. (2016). Figure 1c shows the location of the UWE vault with respect to the main area of collapse in Halema'uma'u crater, along with the centroid moment tensor solutions plotted at the origins of the moment tensor inversion of the three collapse events from 13 to 15 July used in this analysis (USGS, 2018). Not shown are the hundreds of smaller earthquakes that occurred in the time period between the main collapse events.

Whereas we need two different translational sensors to cover the complete range of weak and strong ground motions during the sequence, the very wide sensitivity range of the blueSeis-3A (3×10^{-8} rad/s–0.1 rad/s in a frequency band of 0.01–20 Hz) together with its flat transfer function from DC up to several kHz makes it possible to use just one rotational instrument. In Figure 1d the definition of the rotational coordinate system is shown for clarity. The reader must keep in mind that traditional tilt recordings are defined as positive in the direction of the tilt rather than the corresponding rotation axis. For data analysis and interpretation of

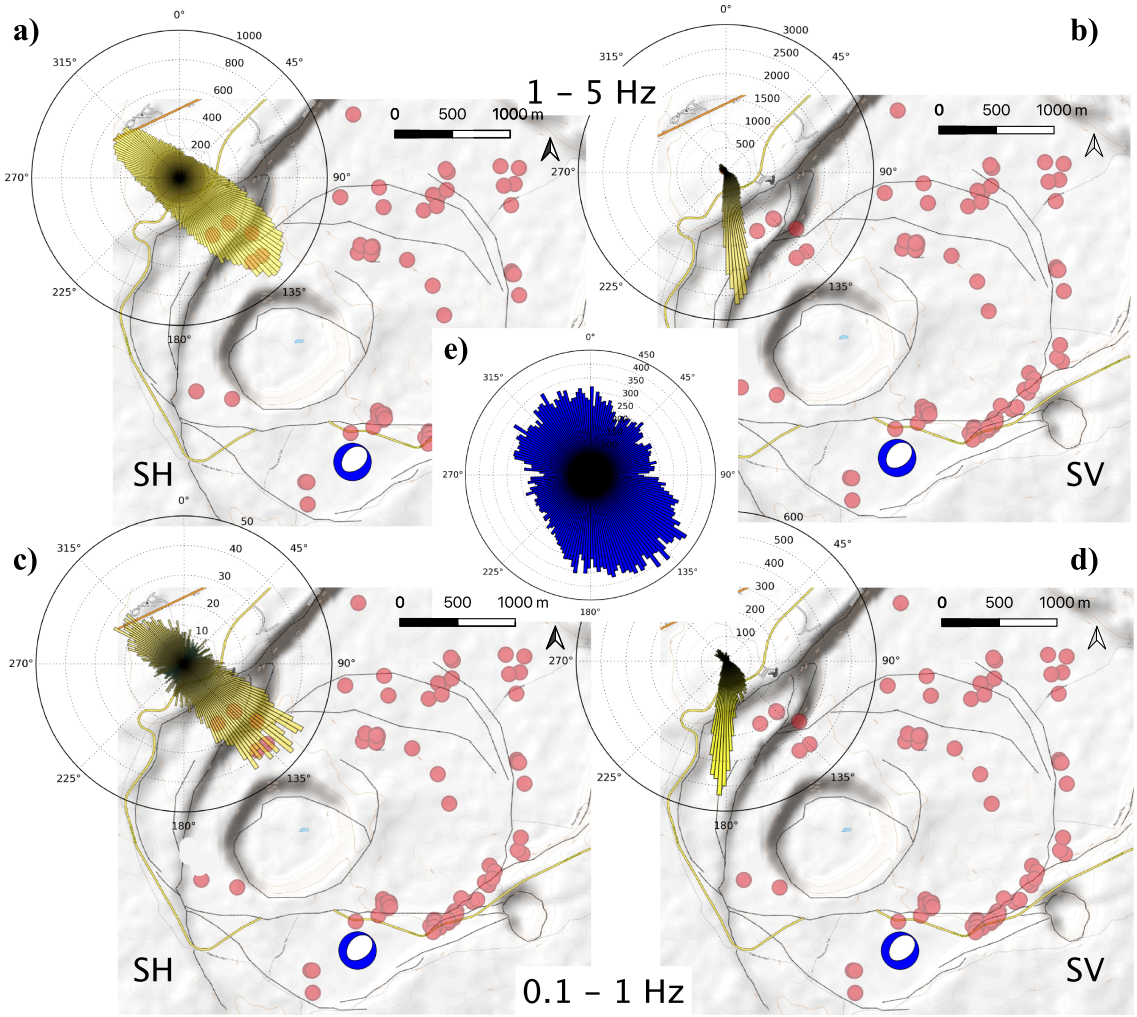

Figure 2. Back azimuth estimation using vertical rotation rate and transverse acceleration after Wassermann et al. (2016) (a and c) as well as simply using horizontal rotation rate (b and d; equation (1)). (a) and (b) represent the directions in the frequency range of 1–5 Hz, while (c) and (d) represents the motion in the frequency range of 0.1–1 Hz. The number in radial direction gives the hits per 2° bin. While (a) and (c) represent pure SH-type motion, (b) and (d) show only SV-type motion. In total roughly four hours of data before and during the 14 July 2018, earthquake is used, which represents the ground motion activity before and during the collapse event. The red circles represent the relocated epicenters of 103 earthquakes occurring during this time period (Shelly & Thelen, 2019), the area of collapse is indicated by gray lines. The small blue rose diagram in (e) gives the directions of the SV-wave dominated wave field after the end of the eruption at 11 August 2018, in the 1 to 5 Hz frequency range for comparison.

events larger than Mw 3.5, we concentrate on the recordings from the EpiSensor accelerometer and the blueSeis-3A data; events smaller than Mw 3.5 utilize recordings from the STS-2 broadband seismometer and the blueSeis-3A data.

3. Analysis and Results

One of the key features of a true rotational motion sensor is its property of acting as a physical S-wave polarizer or filter. As already mentioned, the blueSeis-3A sensor is only sensitive to rotations, i.e., the curl of the wave field, it can record either SH-type waves (on the vertical component) or SV-type waves (on the horizontal components). This property of rotational devices has been used extensively to estimate the back azimuth of an incoming wavefield at a single site with relatively high precision using SH wave polarization (e.g., Hadziioannou et al., 2012; Igel et al., 2007).

Figure 2 shows the source back azimuth estimates for seismicity four hours prior to and during the Mw 5.3 earthquake on 14 July. During this period, roughly 103 earthquakes in the magnitude range of Ml 1–4

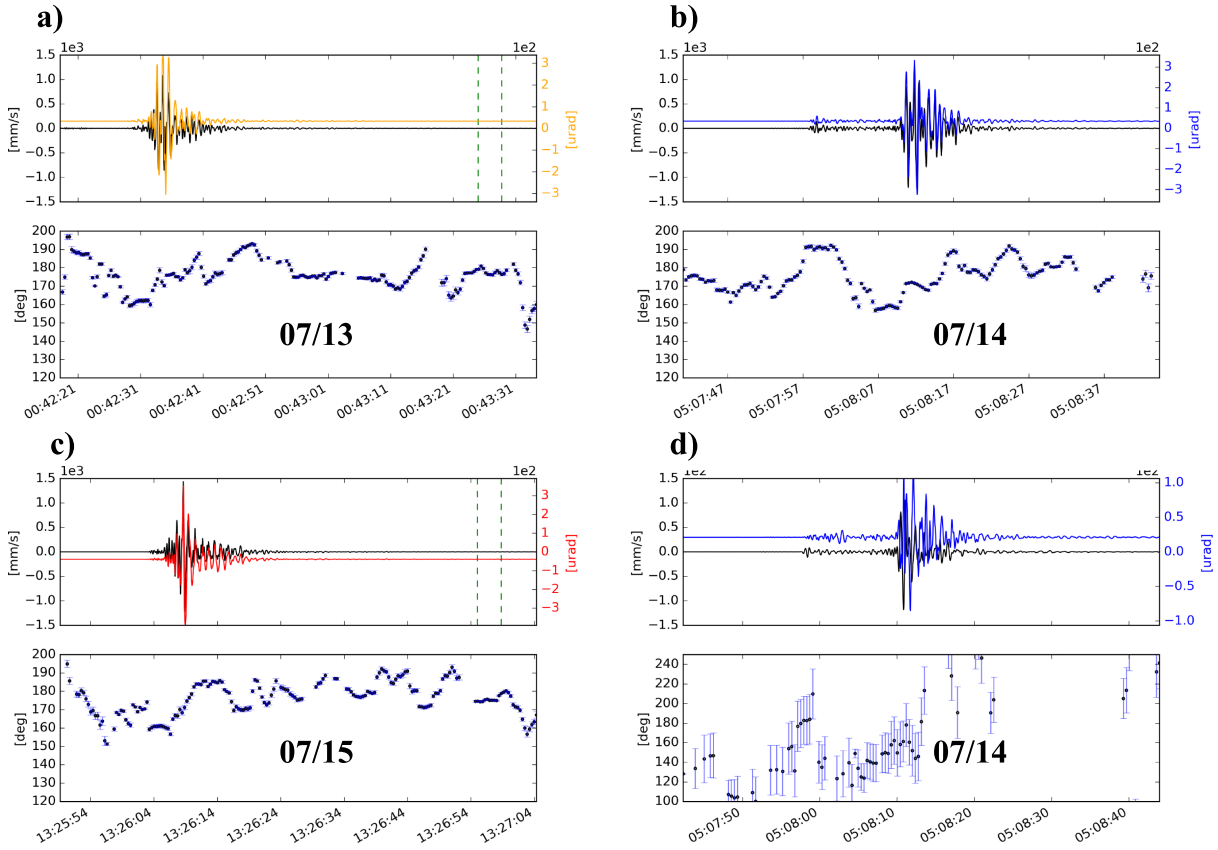

Figure 3. Back azimuth estimation via horizontal rotational motion in the frequency range of 1–5 Hz of the ~Mw 5 events on 13 (a), 14 (b), and 15 July (c) in the corresponding colors of Figure 1c. The upper panels show the radial translational and the corresponding transverse rotation recordings; the lower panels give the time-back azimuth distributions. In (d) the back azimuth estimation using the vertical rotation and transverse velocity of the 14 July event is shown. The dashed green lines in upper panels of (a) and (c) represent the sliding window size used for the analysis. The error bars in (a), (b), and (c) are approximately 4°-wide, while in (d) the average error is 20°.

occurred (Shelly & Thelen, 2019). The figure represents the direction of a superposition of noise as well as ballistic (direct) waves and the coda waves of these earthquakes. Figures 2a and 2c show the result using the orthogonal distance regression technique proposed by Wassermann et al. (2016), which focusses on incoming SH-type waves in the two frequency bands of 0.1–1 and 1–5 Hz. In this case, the direction estimate is solved by a linear equation and a simultaneous optimized rotation of the horizontal components of the translational motion seismograms. In contrast Figures 2b and 2d show the results of direction estimations using the horizontal rotational motion components only (equation (1)) which represents pure SV type of motion:

$$BAz = -\arctan\left(\frac{RotN(t)}{RotE(t)}\right), \tag{1}$$

where BAz stands for the back azimuth and RotN(t) and RotE(t) give the corresponding rotations around the N and E components, respectively. While this estimation procedure simply consists of the application of the arctangent function, the 180° ambiguity in the estimate is resolved by comparing the corresponding acceleration with the rotational seismograms, which need to be in phase if the quadrant is chosen correctly. In all cases the sliding window for this analysis was three times larger than the largest period involved (i.e., 3 s for the 1–5 Hz frequency band) and the width of the directional bins was set to 2°.

Also shown in Figure 2 is the direction of the SV-type wavefield during four hours of 11 August, about 6 days after the termination of the eruption (Figure 2e; Neal et al., 2019). Figures 2b and 2d give a much better azimuthal resolution using horizontal rotational components, but they also show a nearly 35° difference

between SH and SV back azimuth estimates of the wavefield, which requires an explanation. While the SH-type motion seems to originate from an area where most of the smaller relocated earthquakes are clustered (Shelly & Thelen, 2019), the SV-type motion does not point in that direction but towards the south edge of the collapsing caldera. As the blueSeis-3A rotational motion sensor can operate as a north-seeking gyroscope, i.e., a gyro compass with an accuracy better than 2.5° at the geographic location of the UWE vault, a potential misalignment of about 35° can be ruled out. A possible explanation for this discrepancy is the scattering/reflection of SV waves at a structural interface south of the UWE vault. Topographic maps computed after the end of the eruption indeed revealed a very steep and prominent fault scarp in the southwest end of the collapse area (Neal et al., 2019; Figure 2).

Focusing on the three ~Mw 5 events, we can see changing back azimuth varying initially from 170° to 190°, followed by a 160° oriented motion, which finally reverses to 170–190°. Figures 3a, 3b, and 3c correspond to the three ~Mw 5 earthquakes measured on 13, 14, and 15 July. This indicates that the first SV-type motions are pointing roughly towards the centroid origin of the corresponding earthquake, while the SV-coda are again originating from the SSW direction. In contrast to this finding, the direction of the incoming SH-wavefield, being more scattered, shows similar directions but starting with a smaller back azimuth.

Another strong case for using additional components of motion is the possibility to fully reconstruct the movement of a specific point before, during, and after an earthquake. Using a rotational motion sensor with a distinct transfer function, Geng et al. (2019) found that they needed additional geodetic information to fully reconstruct the ground motion history. In contrast to this, the use of fiber optical gyroscope technology without any moving parts makes it possible to correct motions down to DC (i.e., quasistatic movements).

Focusing on the Mw 5.3 event from 14 July, we integrate the rotation rate output of the blueSeis-3A and double integrate the EpiSensor accelerometer data to estimate rotation angle and displacement, respectively. Before integrating the accelerometer data, we first apply a dynamic tilt correction using the horizontal rotational components following a modified version of the technique proposed by Lindner et al. (2016). In Figure 4, various features can be seen—the most unusual one probably being the static rotation around the vertical axis shown in Figure 4a. This is a motion which is not seen by any other sensor without postprocessing data from dense sensor networks (e.g., GNSS). In Figure 4b, a clear static displacement can also be seen even though the observation is blurred by instrumental and numerical noise caused by the double integration of the accelerometer data. While the dynamic tilt correction works down to DC, the transfer function of the EpiSensor and its sensitivity make it impossible to get a more stable solution in the long period range, which is visible in Figure 4 as a sinusoidal low frequency movement.

The main motion of the UWE vault during this earthquake appears to be in a 275° and thus westward direction accompanied by rotations both around the north axis (tilt towards west) and a counter clockwise spin around the vertical axis. In contrast to this tilt and rotation around the vertical axis recorded by the fiber optic gyroscope, the nearby located borehole tiltmeter recorded a roughly 325° orientated tilt (Figure 4a, green lines). While in both cases the tilt of the ground is in an outward direction and thus indicates an inflationary rebound of the crater at the time of the collapse event, the horizontal components of the rotational motion sensor and the borehole tiltmeter show a significant difference in the direction of this tilt. An explanation might be that the difference is caused by a very local effect of strain-tilt coupling (van Driel et al., 2012). The concrete pier on which the blueSeis-3A was installed was designed for optical devices and is elongated in east–west direction. While the pier is more easily tilted in a north–south direction rather than in the recorded east–west direction (N-component of rotation), the estimated rotation and displacement and its corresponding directions indicate a movement that does not only include the pier foundation but the complete UWE vault structure. The described pattern of rotation and displacement is present in all three analyzed ~Mw 5 events.

As a further piece of evidence, we computed synthetic seismograms and rotational motions using the SW4 software package (Petersson & Sjögreen, 2017). The Centroid Moment Tensor (CMT) solution published by the USGS indicates normal faulting with a 30% CLVD, nondouble couple contribution. The reader has to keep in mind that regional and teleseismic seismic data were used to estimate the point approximation of the underlying CMT mechanism. While the amplitudes of the displacement signal seem to be underestimated by the synthetics, the polarity of recorded data and the synthetics do match (Figure 4b). The only exception is the vertical component data, which shows only a very small static displacement in contrast to

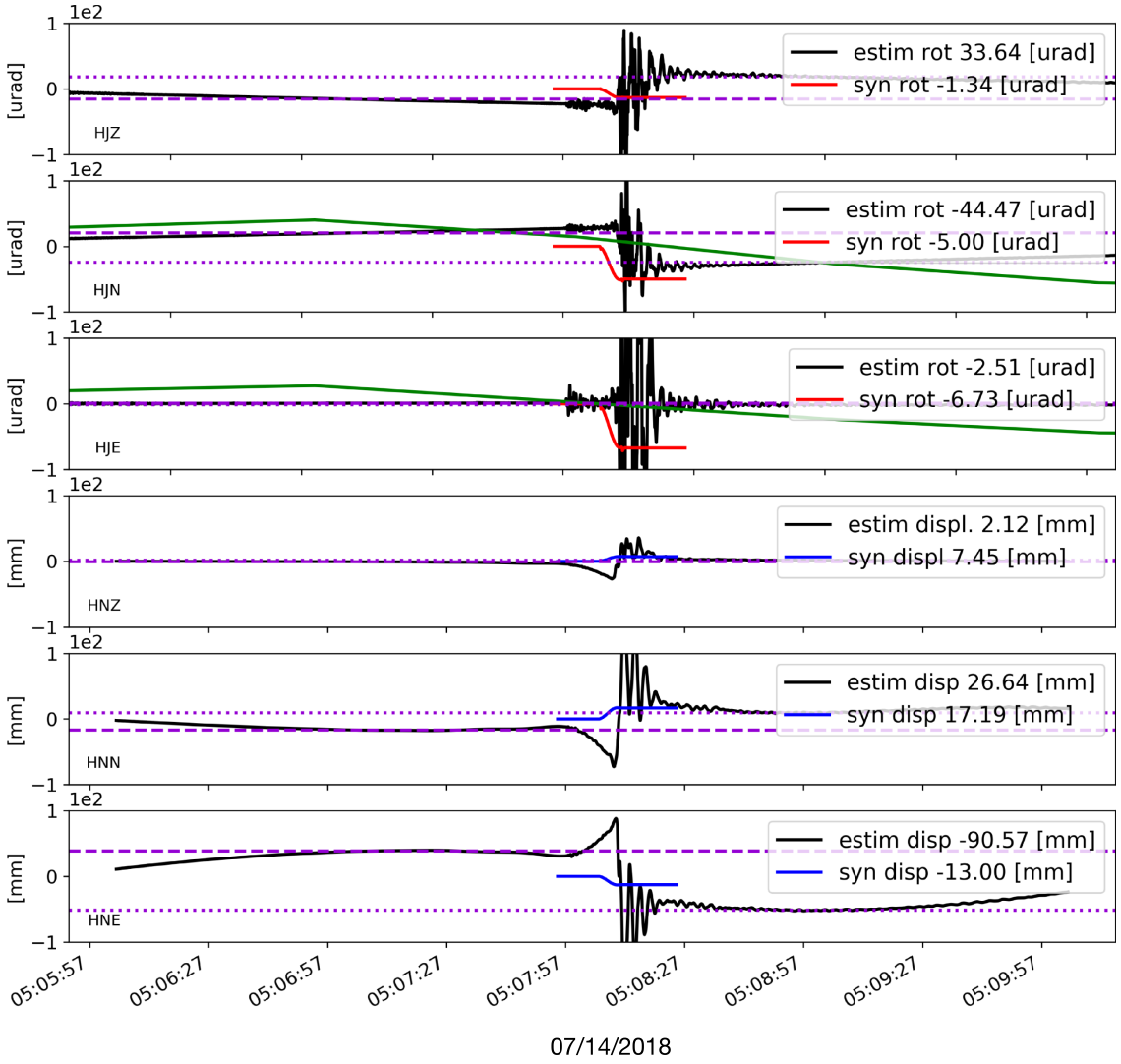

Figure 4. In (a) the angles of rotation are shown (integrated rotation rate). The clear visible static rotation during the Mw 5.3 event on 14 July 2018, is highlighted by dashed violet horizontal lines marking the total rotation of which the amplitude of this static rotation is given in the inset. As a reference, the data of the classical tiltmeter nearby is shown as a green line (note its sampling rate of 1 min). The synthetic rotation motions are shown in red with an exaggeration of factor of 10. In (b) the corresponding displacement traces are shown after tilt correction and double integration of the accelerometer data. The dashed violet lines indicate a static displacement after the earthquake, as well. In this case the synthetic seismograms are shown in blue. The static displacement amplitudes are given in the inset.

the synthetics. This first order match is not seen when using the curl of the wavefield, i.e., the rotation signal (Figure 4a). Neither the amplitude nor the direction of rotation (or tilt) is predicted correctly by the point source approximation. Especially the vertical rotation is not predicted at all neither in the amplitude nor in the sense of rotation. This discrepancy between the synthetics computed using the CMT solution and the measured rotational and translational motion indicates that the estimated motion is either very localized in the near field (i.e., strain-tilt coupling is very effective), and/or the finite source effect is not covered by the simple point source approximation.

4. Conclusions

Summarizing the observation described here, we are left with up to 35° difference between the SH-type and SV-type wavefields, directions which both fit the local geometry of faults or slumping areas. This difference of radiation might be an effect of structural features, scattering, and possible anisotropy. An observation only at one site suffers from nonuniqueness, which can only be resolved by having more distributed measuring

points. The second novel observation is the static rotation around the vertical axis, which is impossible to be observed with data from the borehole tiltmeter. While the tiltmeter shows an outward tilt orientated roughly towards 325°, the fiber optic gyroscope of the blueSeis-3A rotational sensor and the tilt-corrected ground displacements seismograms show an outward tilt and movement oriented roughly 275°. As the orientation of fiber optic gyroscope can be estimated in situ to a precision better than 2.5°, and a 50° misorientation of the borehole instrument can be ruled out as well, the reason for this large discrepancy must lie in the different installation of the two instruments. For future near-field observations, geometrically simple, i.e., symmetric foundations small in size have to be constructed to reduce local strain-tilt effects which might affect the measurements even for borehole instruments.

Adding more axes of motion to the classical observations reveals a very complex motion history for the volcanic collapse earthquakes considered in this paper. A valid question therefore is: does it help to decipher the mechanisms of volcanic events observed in the near field? A bold answer is yes, as we use rotational sensor data to measure finite source effects as well as possible very localized effects due to vault motion, which would normally pass unseen and lead to an incomplete picture of the total motion and partially incorrect interpretations. While six-axis measurements might give us even more riddles to solve, they in turn also might lead us to pose the right questions to be answered in case of near-field recordings of earthquakes and volcanic eruptions.

Acknowledgments
The authors gratefully acknowledge Hawai'i Volcanoes National Park for granting permission to install the instrument despite the closure of the park and to USGS Hawaiian Volcano Observatory seismological staff for facilitating the work. The thoughtful reviews of K. Anderson and A Flinders as well as from two anonymous reviewers and the editor G. Hayes are highly appreciated. JW also wants to acknowledge iXblue for the financial support of this "high risk-high gain" experiment which was planned in a very short time. HI additionally wants to thank the European Research Council for supporting this study with the ERC grant "ROMY." Any use of trade, firm, or product names is for descriptive purposes only and does not imply endorsement by the U.S. Government. Data from the fiber optic gyroscope is available from the IRIS Data Management Center website using the network.station code "HV.UWE" and corresponding channel names "HJ[1,2,3]" (http://ds.iris.edu/mda/HV/UWE/). All plots and analysis were made using the ObsPy Python environment (Beyreuther et al., 2010; Megies et al., 2011). All maps shown were made using QGIS (QGIS development team, 2019).

References

Bernauer, M., Fichtner, A., & Igel, H. (2014). Reducing non-uniqueness in finite source inversion using rotational ground motions. *Journal of Geophysical Research: Solid Earth*, *119*, 4860–4875. https://doi.org/10.1002/2014JB011042

Beyreuther, M., Barsch, R., Krischer, L., Megies, T., Behr, Y., & Wassermann, J. (2010). ObsPy: A Python toolbox for seismology. *Seismological Research Letters*, *81*(3), 530–533. https://doi.org/10.1785/gssrl.81.3.530

Donner, S., Bernauer, M., & Igel, H. (2016). Inversion for seismic moment tensors combining translational and rotational ground motions. *Geophysical Journal International*, *207*(1), 562–570. https://doi.org/10.1093/gji/ggw298

Geng, J., Wen, Q., Chen, Q., & Chang, H. (2019). Six-degree-of-freedom broadband seismogeodesy by combining collocated high-rate GNSS, accelerometers, and gyroscopes. *Geophysical Research Letters*, *46*, 708–716. https://doi.org/10.1029/2018GL081398

Hadziioannou, C., Gaebler, P., Schreiber, U., Wassermann, J., & Igel, H. (2012). Examining ambient noise using co-located measurements of rotational and translational motion. *Journal of Seismology*, *16*(4), 787–796. https://doi.org/10.1007/s10950-012-9288-5

Igel, H., Cochard, A., Wassermann, J., Flaws, A., Schreiber, U., Velikoseltsev, A., & Pham Dinh, N. (2007). Broad-band observations of earthquake-induced rotational ground motions. *Geophysical Journal International*, *168*(1), 182–196. https://doi.org/10.1111/j.1365-246X.2006.03146.x

Lindner, F., Wassermann, J., Schmidt-Aursch, M. C., Schreiber, K. U., & Igel, H. (2016). Seafloor ground rotation observations: Potential for improving signal-to-noise ratio on horizontal OBS components. *Seismological Research Letters*, *88*(1). https://doi.org/10.1785/0220160051

Megies, T., Beyreuther, M., Barsch, R., Krischer, L., & Wassermann, J. (2011). ObsPy-What can it do for data centers and observatories? *Annals of Geophysics*, *54*(1), 47–58. https://doi.org/10.4401/ag-4838

Neal, C. A., Brantley, S. R., Antolik, L., Babb, J. L., Burgess, M., Calles, K., et al. (2019). The 2018 rift eruption and summit collapse of Kīlauea Volcano. *Science*, *363*(6425), 367–374. https://doi.org/10.1126/science.aav7046

Petersson, N. A., & Sjögreen, B. (2017). SW4 (Seismic Waves, 4th order) v2.0, Computational Infrastructure for Geodynamics, Davis, CA. https://doi.org/10.5281/zenodo.1045297

QGIS Development Team (2019). QGIS Geographic Information System. Open Source Geospatial Foundation Project. http://qgis.osgeo.org

Shelly, D. R., & Thelen, W. A. (2019). Anatomy of a caldera collapse: Kīlauea 2018 summit seismicity sequence in high resolution. *Geophysical Research Letters*, *46*, 14,395–14,403. https://doi.org/10.1029/2019GL085636

USGS (2018). publicID = "quakeml:earthquake.usgs.gov/fdsnws/event/1/query.quakeml?starttime = 2018-07-13 T000000&endtime = 2018-07-15 T230000&maxlatitude = 19.438&minlatitude = 19.379&maxlongitude = -155.243&minlongitude = -155.303&minmagnitude = 5&includeallorigins = true&includeallmagnitudes = true&orderby = time", last visited: 02/13/2020.

USGS Hawaiian Volcano Observatory (HVO) (1956). Hawaiian Volcano Observatory Network. International Federation of Digital Seismograph Networks. Dataset/Seismic Network. https://doi.org/10.7914/SN/HV

van Driel, M., Wassermann, J., Nader, M. F., Schuberth, B. S. A., & Igel, H. (2012). Strain rotation coupling and its implications on the measurement of rotational ground motions. *Journal of Seismology*, *16*(4). https://doi.org/10.1007/s10950-012-9296-5

Wassermann, J., Wietek, A., Hadziioannou, C., & Igel, H. (2016). Toward a single-station approach for microzonation: Using vertical rotation rate to estimate love-wave dispersion curves and direction finding. *Bulletin of the Seismological Society of America*, *106*(3). https://doi.org/10.1785/0120150250